Sodium metal hybrid capacitors based on nanostructured carbon materials

Hyo Won Kwak[a,1], Min Eui Lee[b,1], Hyoung-Joon Jin[b,**], Young Soo Yun[c,*]

[a] Department of Forest Sciences, Seoul National University, Seoul, 08826, South Korea
[b] Department of Polymer Science and Engineering, Inha University, Incheon, 22212, South Korea
[c] Department of Chemical Engineering, Kangwon National University, Samcheok, 25913, South Korea

HIGHLIGHTS

- Sodium metal anode was designed using catalytic carbon nanotemplates (C-CNTPs).
- Nanoporous pyroproteins (N-PPts) were prepared as a cathode for sodium ion storage.
- Sodium metal hybrid capacitors (SMHCs) based on the two electrodes were designed.
- The SMHCs can deliver a high specific energy of ~ 237.7 Wh kg^{-1} at ~ 462 W kg^{-1}.

GRAPHICAL ABSTRACT
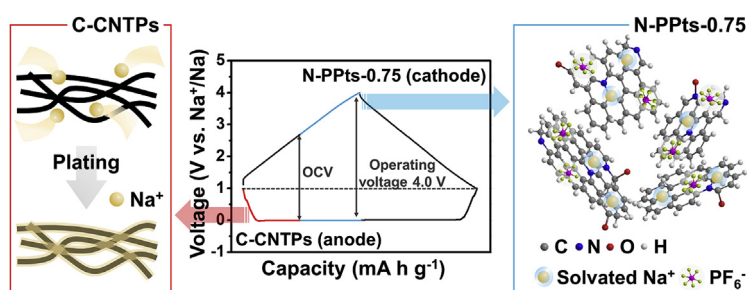
ABSTRACT

In this study, sodium metal hybrid capacitors (SMHCs) composed of a metal anode and capacitive cathode are reported for the first time. The sodium metal anode was designed using catalytic carbon nanotemplates (C-CNTPs) and exhibited highly reversible sodium metal plating/stripping behaviors with an average Coulombic efficiency of $\sim 100\%$ over 1000 galvanostatic cycles and significantly low cell-to-cell variations. Further, nanoporous pyroproteins (N-PPts) with a specific surface area of ~ 4216 m^2 g^{-1} and pore volume of 1.937 cm^3 g^{-1} were fabricated as the capacitive cathode, exhibiting a high specific capacity of 168 mA h g^{-1}, high rate capability of 0.5–10 A g^{-1}, and stable cycling performance over 1000 cycles. The SMHCs based on C-CNTPs/N-PPts were operated in a voltage window of 1.0–4.0 V, delivering a high specific energy of ~ 237.7 Wh kg^{-1} at ~ 462 W kg^{-1} and a maximum power of ~ 4800 W kg^{-1} at ~ 66.7 Wh kg^{-1}. In addition, stable cycling performance was maintained during 500 cycles, with a capacity retention of $\sim 82\%$.

1. Introduction

Sustainable and green energy systems (GESs) are eco-friendly clean cycles for energy generation and consumption in modern society [1,2]. Clean energy sources include sunlight, wind, biomass, and tides/waves; however, on-demand supply of clean energy is limited by uncontrolled power generation [1,2]. Moreover, the rapid development in the electric vehicle industry has led to an increase in energy consumption, and hence, the demand for high-performance power sources has increased [3]. Therefore, a mass-scalable energy storage system (ESS) with high energy/power characteristics and long-term cycling stability is necessary to achieve GESs [4]. Na-ion storage devices are the main candidates for application in large-scale ESSs because of the abundant and ubiquitous nature of Na and because the properties of Na ions are

similar to those of Li ions [5]. However, Na ions are ca. 55% larger and 330% heavier and have a 0.33 eV higher electropotential, leading to poor specific energy and solid-state diffusion kinetics in host materials [5–7]. An innovative ESS beyond conventional intercalation chemistry is required to overcome these obstacles.

Na metal is an ideal anode material owing to its high theoretical capacity of ~ 1166 mA h g^{-1} and low redox potential (-2.71 V versus standard hydrogen electrode). Therefore, the development of Na metal anodes has recently attracted intensive interest [8–10]. However, dendritic metal growth and infinite volume changes in the metal anodes cause serious safety issues, low Coulombic efficiency (CE), and poor cycling stability [11–13]. To address these issues, several technical approaches such as introducing catalytic templates [10,13,14], engineering of an electrolyte system [12,15,16], and surface stabilization [17,18] have been proposed [19]. Cui's group reported that a glyme-based electrolyte enables highly reversible and non-dendritic Na metal plating/stripping cycles at room temperature [8]. It was also reported that carbon-based template materials can guide uniform metal nucleation without dendritic metal formation [13,20,21]. These reports suggest that Na metal anodes can be practically achieved through a combination of glyme-based electrolytes and catalytic carbon nanotemplates (C-CNTPs). In our previous study, a feasible Na metal anode was realized by the synergistic effect of these techniques, exhibiting stable cycling behavior over 1000 cycles with a CE of $\sim 99.9\%$ and high rate capability of ~ 4 A g^{-1} [10]. The reason for the high electrochemical performance of C-CNTPs was their well-ordered graphitic structure, which significantly retarded the degradation of unstable carbon active sites, leading to the long cycle lifetimes. A high-performance Na metal anode may facilitate a more powerful ESS when combined with well-defined energy storage technologies.

Carbon-based porous materials (CPMs) have been widely used as electrode materials for supercapacitors [22–24]. CPMs store charge by forming an electrochemical double layer (EDL) through physical adsorption and desorption of charge on their internal surface [22]. Their capacitive charge storage characteristics are very fast and highly reversible, showing great power capability and long cycle lifetimes [22]. In addition, it has been reported that sub-nanometer-/nanometer-scale pores can increase charge storage efficiency by preventing overscreening and geometrically confining the charges [25–28]. Kim et al. reported that hierarchically nanoporous pyropolymers exhibit significantly high electrochemical performance in a wide operating voltage window due to their amphicharge (lithium ion and anion) storage behavior [29]. Also, Cho et al. realized high-performance sodium-ion supercapacitors using nanoporous pyroprotein (N-PPt) electrodes [30]. Hence, CPMs possessing high specific surface areas and well-tailored nanopores can deliver a much larger charge within a very short time, thus proving to be a suitable counterpart for sodium metal anodes.

In this study, we report high-performance sodium metal hybrid capacitors (SMHCs) based on C-CNTPs and N-PPts as the metal anode and capacitive cathode, respectively. Sericulture byproduct-induced N-PPts showed a remarkably high specific surface area of ~ 4216 m^2 g^{-1} and a large concentration of nitrogen dopants of ~ 5.7 at.%, leading to a high specific capacity of 168 mA h g^{-1} in a cathodic voltage window of 1.0–4.2 V vs. Na$^+$/Na, high rate capability at 4 A g^{-1} with a capacity retention of $\sim 62\%$, and good cycling performance over 1000 cycles. As its counterpart, C-CNTPs with a well-ordered graphitic structure were designed from bacterial cellulose (BC) by controlled pyrolysis to aid reversible sodium metal deposition/stripping. The C-CNTP-based sodium metal anodes showed a high average CE of $\sim 99.9\%$ over 1000 continuous cycles. The SMHCs were assembled after pre-cycling to achieve energy and power balance between both electrodes, and they exhibited a high specific energy of 237.7 Wh kg^{-1} at 462 W kg^{-1} and high power of 4800 W kg^{-1} at 66.7 Wh kg^{-1}, with a capacity retention of $\sim 82\%$ after 500 cycles.

2. Experimental

Preparation of N-PPts and C-CNTPs: To prepare N-PPts, silk sericin was extracted by autoclaving cocoons of *Bombyx mori* silk for 1 h at 120 °C. The final concentration of the extracted silk sericin solution was ~ 1.0 wt%. KOH (1, 2, 3, and 4 g) was added to 400 g of the silk sericin solution. The silk sericin/KOH mixture was gently stirred for 30 min and then cast on Teflon dishes. The cast solutions were dried in a convection oven at 60 °C for 2 days. The obtained silk sericin/KOH mixture films were heated from room temperature to 800 °C for 2 h at a heating rate of 10 °C min^{-1} under a nitrogen flow of 200 mL min^{-1}. The resulting carbonaceous materials were washed with distilled water and ethanol and dried in a vacuum oven at 30 °C. BC pellicles were produced by *Acetobacter xylinum* BRC 5 in a Hestrin and Schramm medium using a previously reported method [31]. The solvent from the as-obtained BC hydrogels was replaced with tert-butanol, and the hydrogels were freeze-dried at -45 °C and 4.5 Pa for 72 h. The freeze-dried BC hydrogels were heated at 5 °C min^{-1} to 800 °C in a tube furnace under a nitrogen flow of 200 mL min^{-1} and maintained at 800 °C for 2 h. To prepare the C-CNTPs, the obtained carbonaceous materials were heated to 2400 °C at 5 °C min^{-1} under Ar using a graphitization furnace (ThermVac, Korea) and maintained at 2400 °C for 2 h. The asprepared samples were used without further treatment.

Characterization: The morphologies of N-PPts and C-CNTPs were examined by FE-SEM (S-4300, Hitachi, Japan) and FE-TEM (JEM2100F, JEOL, Japan). Raman spectra of the samples were recorded using a continuous-wave linearly polarized laser (532 nm, 2.41 eV, 16 mW). The laser beam was focused by a 100× objective lens, resulting in a spot diameter of ~ 1 μm. The acquisition time and number of cycles to collect each spectrum were 10 s and 3, respectively. XRD (Rigaku DMAX 2500) analysis was performed using Cu-Kα radiation ($\lambda = 0.154$ nm) at 40 kV and 100 mA. The surface properties of the samples were examined by XPS (PHI 5700 ESCA, USA) using monochromatic Al-Kα radiation (hν = 1486.6 eV). The porous structures of the samples were analyzed by nitrogen adsorption and desorption isotherms obtained using a surface area analyzer and a porosimetry analyzer (ASAP 2020, Micromeritics, USA) at -196 °C.

Electrochemical characterization: The electrochemical performances of the N-PPts, C-CNTPs, and SMHCs were characterized using a Wonatech automatic battery cycler and CR2032-type coin cells. For half-cells, coin cells were assembled in a glove box filled with argon using N-PPts and C-CNTPs as the working electrode and metallic Na foils as the reference and counter electrodes. NaPF$_6$ (Aldrich, 98%) was dissolved in a solution of DEGDME to a concentration of 1 M and used as the electrolyte for both metal anode and capacitive cathode. A glass microfiber filter (GF/F, Whatman) was used as the separator. The C-CNTPs were punched as 1/2-inch-diameter holes and used as the working electrode without a substrate, conductive agent, and binder. For the N-PPts, the working electrodes were prepared by mixing the active material (90 wt%) with polyvinylidene difluoride (10 wt%) in N-methyl-2-pyrrolidone. The resulting slurries were uniformly cast on an Al foil, and the resulting electrodes were dried at 120 °C for 2 h and rollpressed. The active material mass loading was ~ 1 mg cm^{-2}, and the total electrode weight was 2–3 mg for both metal anode and capacitive cathode. For the SMHCs, the C-CNTPs were pre-sodiated by extraction in a glove box under argon and then assembled with N-PPts-0.75. The same electrolyte and separator were used, and the total electrode weight (both anode and cathode) was 3–4 mg.

3. Results and discussion

For the capacitive charge storage cathode, N-PPts were prepared from sericin by a one-step pyrolysis and activation process with potassium hydroxide. The pyrolysis temperature was fixed as 800 °C, while the concentration of potassium hydroxide was varied from 25 to 100 wt% with respect to the sericin weight for chemical activation.
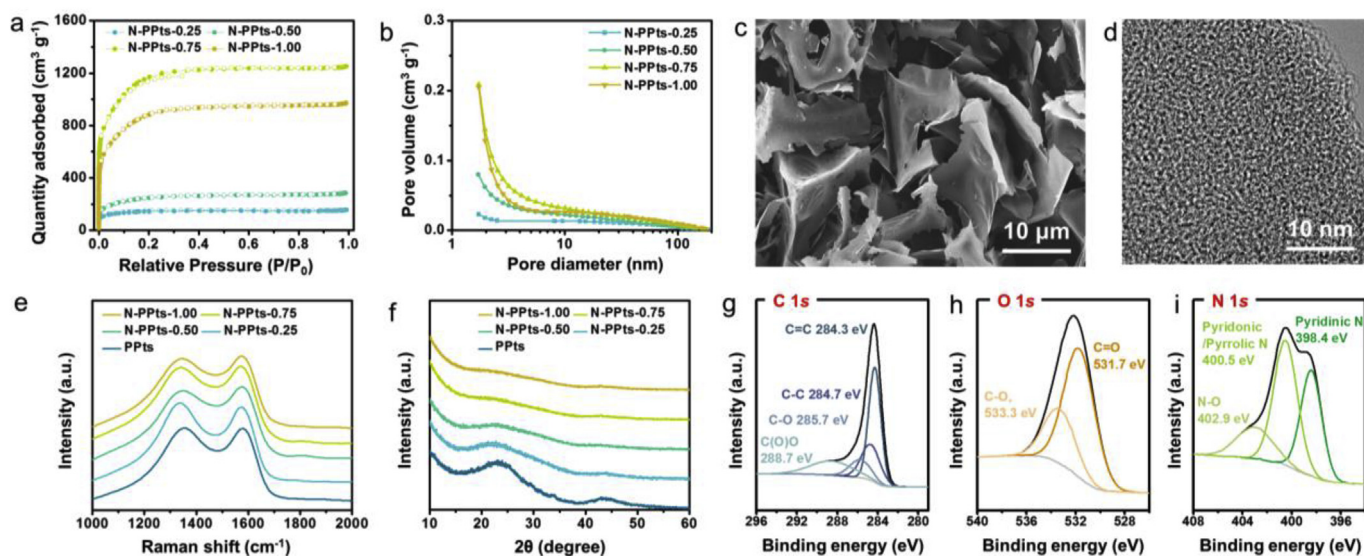
Fig. 1. Material properties of N-PPts. (a) Nitrogen adsorption and desorption isotherm curves and (b) pore size distribution data. (c) FE-SEM and (d) high-resolution FE-TEM images. (e) Raman spectra and (f) XRD patterns. XPS (g) C 1*s*, (h) O 1*s*, and (i) N 1*s* spectra.

According to the concentrations of the activation agent, the pore structures and carbon microstructures of N-PPts were significantly transmuted. As shown in Fig. 1(a), the nitrogen adsorption and desorption isotherm curves of N-PPts showed a microporous structure similar to the International Union of Pure and Applied Chemistry (IUPAC) Type-I shape. The structure showed a dramatically increased nitrogen adsorbed quantity at low relative pressure (< 0.02), indicating a large monolayer adsorption area. The largest monolayer adsorption area was observed for N-PPts-0.75 (75 wt% of KOH), indicating that this sample had the highest number of micropores. The following logarithmic function-like increase sections ($0.02 < P < 0.25$) of N-PPts indicated multi-layered adsorption of nitrogen molecules by pore filling, with no hysteresis between the adsorption and desorption curves. The hysteresis-free multi-layered nitrogen adsorption mainly occurred in a few nanometer-scale pores, which is also remarkable in N-PPts-0.75. The pore diameter vs. pore volume plot [Fig. 1(b)] clearly exhibits the pore size distribution of N-PPts, where most of the pore volume was concentrated in a few nanometer-scale pores. Further, N-PPts-0.75 showed the largest pore volume with a broad pore size distribution. Its specific surface area and nanopore volume were $4216 \, m^2 \, g^{-1}$ and $1.937 \, cm^3 \, g^{-1}$, respectively, which is the highest surface area achieved thus far for samples prepared by a simple activation process. The specific textural properties of N-PPts are listed in Table S1.

The morphology and carbon microstructure of N-PPts-0.75 were characterized by field-emission scanning electron microscopy (FE-SEM) and field-emission transmission electron microscopy (FE-TEM), respectively, as shown in Fig. 1(c and d). Several irregularly shaped micrometer-scale particles were observed in all samples [Fig. 1(c) and Fig. S1]. In addition, a highly amorphous microstructure without long-range graphitic ordering was observed in the high-resolution FE-TEM image of N-PPts-0.75. Further details of the carbon microstructures of N-PPts were investigated by Raman spectra and X-ray diffraction (XRD) patterns [Fig. 1(e and f)]. The Raman spectra showed a broad peak pair assigned as D and G bands at ~ 1350 and $\sim 1578 \, cm^{-1}$, respectively [Fig. 1(e)]. The two characteristic bands originated from the disordered A_{1g} breathing mode and the E_{2g} vibration mode of hexagonal carbon structures for D and G peaks, respectively [32]. The broad and fused bands composed of the similar D to G peak intensities (I_D/I_G) indicated that their carbon microstructures were highly defective, and their aromatic polyhexagonal domains had a size of a few nanometers. The two-dimensional carbon building blocks known as basic structural units

(BSUs) were distorted with defects, leading to poor stacking of the BSUs. Therefore, the XRD patterns of the N-PPts showed very broad (002) graphite peaks [Fig. 1(f)]. The broad graphite peaks gradually disappeared with increasing concentration of the activation agent, indicating that the BSU stacking had fully collapsed. The patulous carbon BSUs generated numerous nanopores with sizes ranging from the sub-nanometer scale to several nanometers depending on the concentration of the activation agent. The Brunauer–Emmett–Teller (BET) characterization results revealed that the optimal KOH concentration was ~ 75 wt%, resulting in the highest specific surface area and a nanoporous structure in the N-PPts [Table S1].

The surface properties of N-PPts were characterized by X-ray photoelectron spectroscopy (XPS), as shown in Fig. 1(g–i) and Fig. S2. In the C 1s spectrum, sp^2 C=C bonding was observed, which was much stronger than the sp^3 C–C bonding, indicating the presence of a well-developed large conjugated structure [Fig. 1(g)]. Minor C–O, C–N, and C=O configurations were also observed for the N-PPts, which were confirmed in the O 1s and N 1s spectra [Fig. 1(h and i)]. Oxygen atoms were mainly composed of two functional groups, carbonyl and ether structures, and their configurations were similar in all the N-PPts [Fig. 1(h) and Fig. S2]. Nitrogen atoms were mainly doped in the hexagonal carbon structures by substitutional doping and appeared as pyridonic and pyridinic N and nitrogen oxide (N–O) groups [Fig. 1(i)]. The nitrogen groups on the carbon structures could modify their conduction band to a larger electron donor state by electron doping, leading to enhanced electrical conductivity and quantum capacitance [33,34]. Although the nitrogen content of the sericin-induced pyroproteins gradually decreased with increasing concentration of the activation agent, considerable quantities of nitrogen remained in N-PPts: 6.78, 6.24, 5.70, and 2.73 at.% in N-PPts-25,-50, -75, and -100, respectively. In addition, the C/N and C/O ratios of N-PPts-75 were 14.85 and 8.73, respectively. More detailed information of the heteroatom compositions of N-PPts is provided in Table S1.

C-CNTPs were prepared from freeze-dried BC pellicles by simple heating at 2400 °C without further treatment to guide the reversible sodium metal plating/stripping process. The C-CNTPs showed a three-dimensional macroporous web structure composed of numerous entangled nanofiber-like components [Fig. 2(a)]. As shown in Fig. 2(b), C-CNTPs had well-ordered graphitic nanoribbon structures with a few-layered graphene stack. The highly developed graphitic structure of the C-CNTPs was also confirmed in the Raman spectrum [Fig. 2(c)]. The Raman spectrum of the C-CNTPs exhibited narrow and split D and G
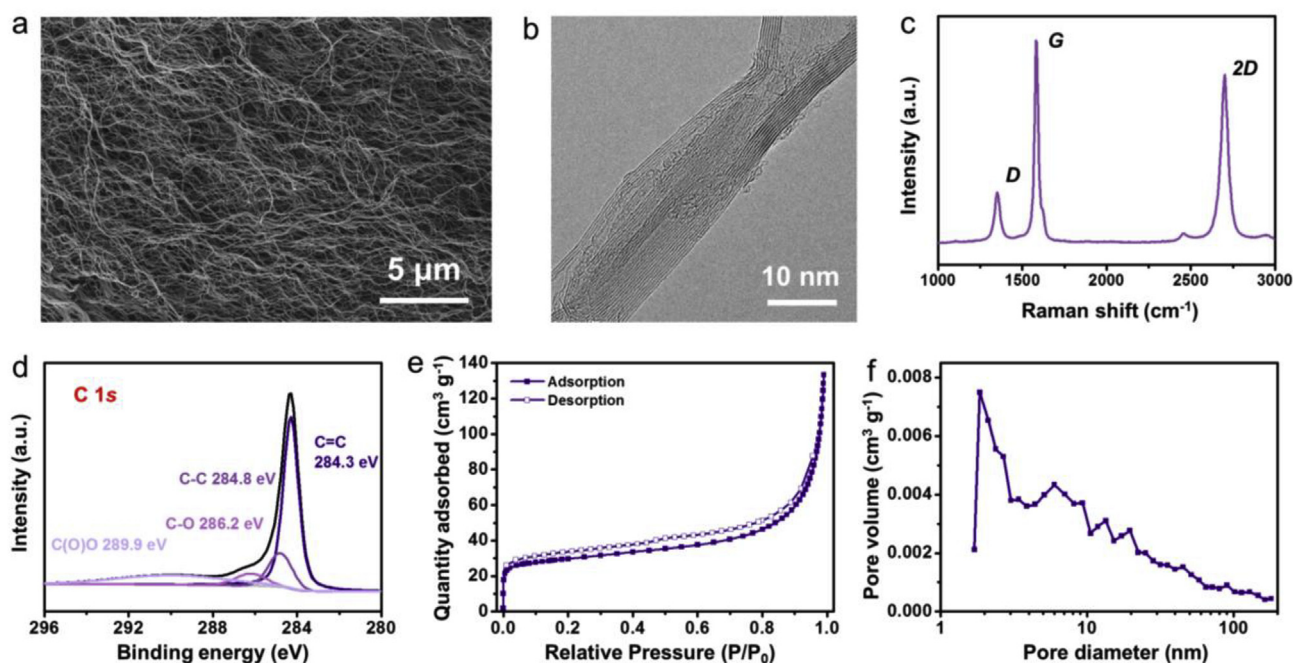
Fig. 2. Material properties of C-CNTPs. (a) FE-SEM and (b) high-resolution FE-TEM images. (c) Raman and (d) XPS C 1*s* spectrum. (e) Nitrogen adsorption and desorption isotherm curves and (f) pore size distribution data.

bands with a significantly low I_D/I_G value of ~0.2, indicating that the ordered graphitic structures had a size greater than ~10 nm. In addition, the Raman spectrum of the C-CNTPs showed a sharp 2D band at ~2700 cm^{-1}, representing three-dimensionally ordered graphitic structures [32]. The XPS C 1s spectrum confirmed the well-ordered graphitic structures of the C-CNTPs [Fig. 2(d)]. A pair of sharp sp [2] C=C bonding and minor sp [3] C–C bonding peaks were observed at 284.3 and 284.8 eV, respectively, and an insignificant peak for the C=O group was detected at 289.9 eV. The oxygen content of the C-CNTPs was negligible, where the C/O ratio was 226. The pore structure of the C-CNTPs was characterized by the nitrogen adsorption and desorption isotherm curve [Fig. 2(e)]. The isotherm curve of C-CNTPs was IUPAC Type-II, i.e., macroporous structures with a broad pore size distribution, indicating a hierarchically porous structure [Fig. 2(f)].

The electrochemical properties of N-PPts and C-CNTPs were characterized by 2032-type coin cells with Na metal foils as the reference and counter electrodes in an electrolyte of 1 M NaPF$_6$ dissolved in diethylene glycol dimethyl ether (DEGDME). As shown in Fig. 3(a), N-PPts-0.75 showed a nearly rectangular cyclic voltammogram at scan rates of 5, 10, and 20 mV s^{-1} in a wide voltage window of 1.0–4.2 V, indicating its capacitive charge storage behavior. In the large voltage window, both cations and anions acted as charge carriers in different voltage sections based on the open circuit voltage (2.7 V vs. Na$^+$/Na) [29]. The amphicharge-storable N-PPts had a high capacity in all voltage sections [Fig. 3(b)]. Therefore, there was no voltage hysteresis, indicating highly reversible charge storage performance based on EDL formation [Fig. 3(b)]. The specific capacity of N-PPts-0.75 reached 168 mA h g^{-1} at a current rate of 0.5 A g^{-1} and gradually decreased with increasing current rate [Fig. 3(c)] and was approximately 62 mA h g^{-1} at a current rate of 10 A g^{-1}. The galvanostatic charge/discharge profiles demonstrated very fast charge storage kinetics for N-PPts-0.75 [Fig. 3(c)]. The specific capacities and rate capabilities of the N-PPts including N-PPts-0.75 are depicted in Fig. 3(d). N-PPts-0.75 showed the highest specific capacity among all samples, which could be due to its high specific surface area of 4216 m^2 g^{-1} and nanoporous microstructure containing a considerable amount of nitrogen dopants.

Galvanostatic sodium metal deposition/stripping cycles of the C-CNTPs were tested with a cut-off capacity of 0.5 mA h cm^{-2} for

discharge and cut-off voltage of 1 V for charge. As shown in Fig. 4(a), the voltage profile characterized at a low current rate of 50 μA cm^{-2} showed voltage overshooting in the early discharge sections below 0 V, which could be due to a nucleation barrier of electrochemically deposited sodium metal. Overpotential could be calculated by the voltage gap between the peak point of the voltage overshoot and plateau region. The overpotential was about 9.7 mV, which was significantly smaller than that of an Al electrode (25 mV) [Fig. S3]. Although the overpotential gradually increased with increasing current rate, a 2.5-fold larger overpotential (~24 mV) was observed at an 80-fold higher current rate (4 A cm^{-2}), indicating the excellent rate capability of the C-CNTPs [Fig. 4(b)]. The average CEs of the C-CNTPs at different current rates and their standard deviations are depicted in Fig. 4(c). At current rates of 0.5, 1, and 2 mA cm^{-2}, an average CE of 99.9% was achieved over 200 cycles. In addition, CE deviations tested using more than 10 different cells were ~0.83%, ~0.51%, ~0.63%, ~0.61%, and 0.71% at 0.2, 0.5, 1, 2, and 4 mA cm^{-2}, respectively, indicating significantly low cell-to-cell variations. Another notable result was the highly stable cycling behavior of the C-CNTPs [Fig. 4(c)]. Galvanostatic sodium metal plating/stripping cycling at 1 mA cm^{-2} was highly stable over 1000 cycles, with an average CE of nearly 100% [Fig. 4(d)]. Na metal nucleation could be described by the following first-order linear equation:

$$\frac{dN}{dt} + AN = AN_0, \quad N(0) = 0 \tag{1}$$

where N_0, N, and A denote the number density of the active sites, density of nucleated particles, and nucleation rate, respectively [35]. Three different growth regimes could be distinguished by the variations in the ratio of the characteristic times of diffusion $1/DN_0$ and charge transfer $1/k_GN_0^{1/2}$ (D and k_G denote the diffusion coefficient and charge transfer kinetics constant, respectively): kinetic control ($k_G/DN_0^{1/2} \ll 1$), mixed kinetic–diffusion control ($k_G/DN_0^{1/2}$–1), and diffusion control ($k_G/DN_0^{1/2} \gg 1$) [35]. The diffusion-controlled growth is generally accompanied by the formation of dendritic structures, while the kinetic-controlled growth leads to identical (homogeneous) metal growth on the overall surface. Therefore, the presence of numerous active sites on the C-CNTPs could guide kinetic-controlled growth, causing
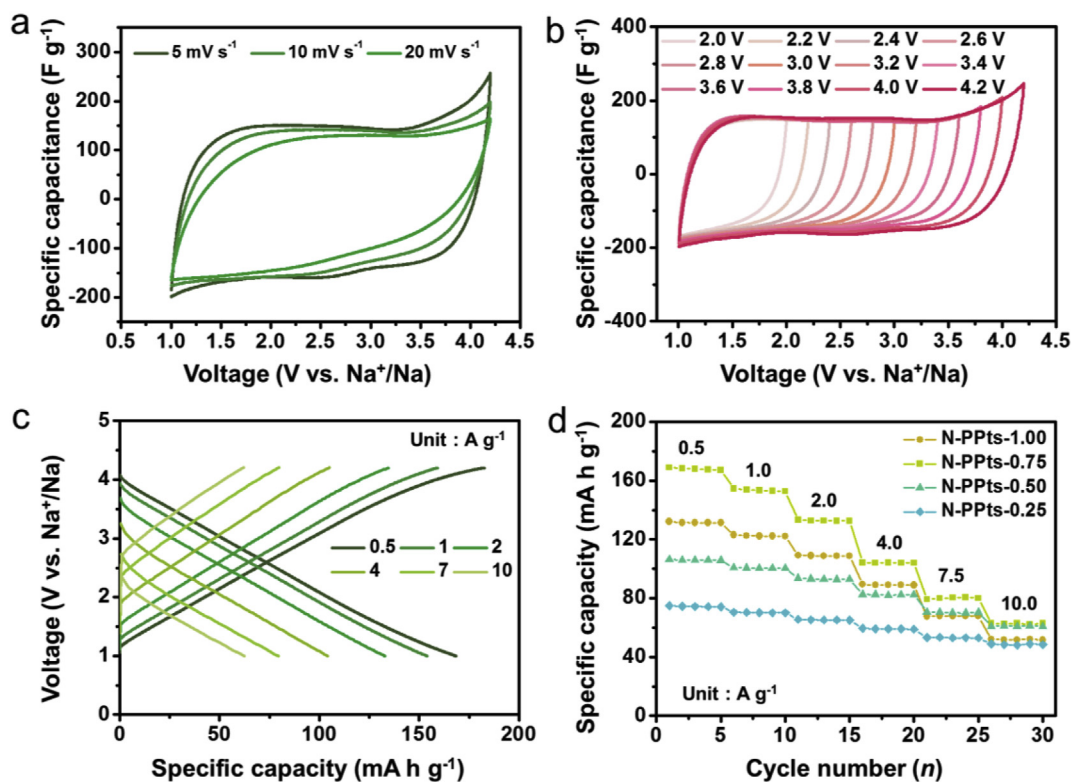
Fig. 3. Electrochemical properties of N-PPts in an electrolyte of 1 M NaPF$_6$ dissolved in DEGDME. Cyclic voltammograms (a) at different current rates in a voltage window of 1.0–4.2 V and (b) at 5 mV s^{-1} in different voltage ranges from 1.0 to 4.2 V with intervals of 0.2 V. (c) Galvanostatic charge/discharge profiles at various current densities from 0.5 to 10 A g^{-1} and (d) rate capabilities of N-PPts at different current rates in the voltage window 1.0–4.2 V.
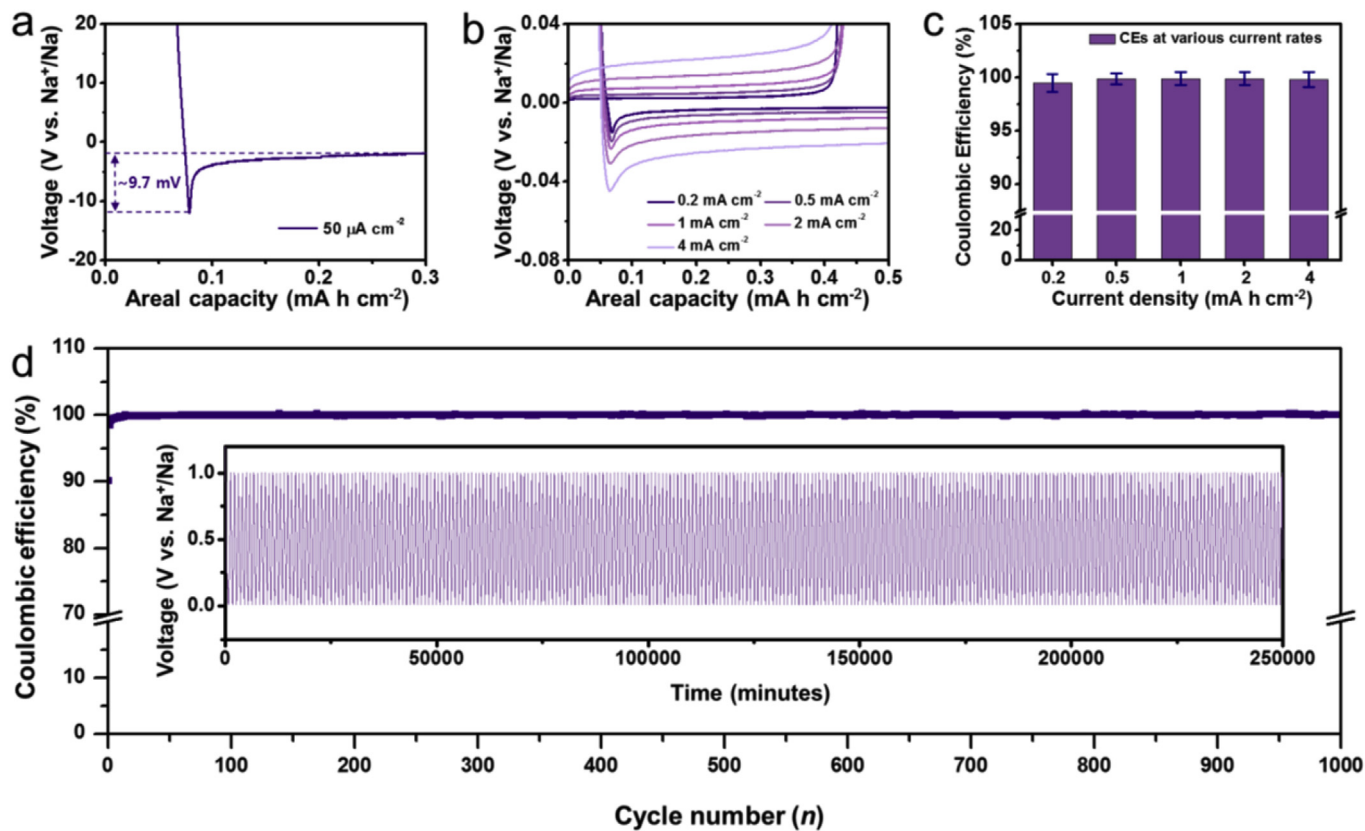

Fig. 4. Electrochemical properties of C-CNTPs in an electrolyte of 1 M NaPF$_6$ dissolved in DEGDME. (a) Galvanostatic sodium metal plating profiles at a current rate of 50 μA cm^{-2} and (b) galvanostatic sodium metal plating/stripping profiles at different current rates from 0.2 to 4 mA cm^{-2}. (C) CEs and CE deviations at different current rates using more than 10 cells. (d) Cycling behavior of sodium metal plating/stripping at 1 mA cm^{-2} and inset is time vs. voltage plot for the cycling data.
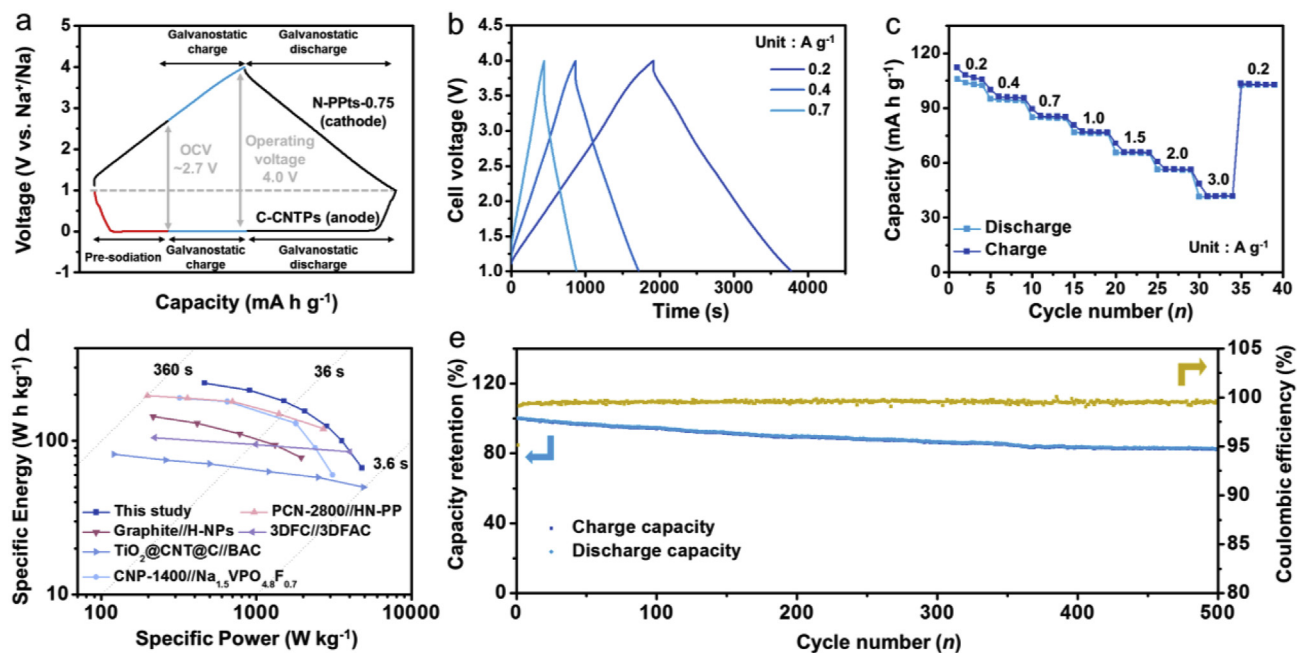
Fig. 5. Electrochemical performance of SMHCs based on C-CNTPs//N-PPts-0.75 in an electrolyte of 1 M NaPF$_6$ dissolved in DEGDME in a voltage window of 1.0–4.0 V. (a) Schematic of initial cell preparation process. (b) Galvanostatic charge/discharge profiles at current rates of 0.2, 0.4, and 0.7 A g^{-1}. (c) Rate capabilities at different current rates. (d) Ragone plots of various energy storage devices including C-CNTPs//N-PPts-0.75. (e) Cycling performance at 0.5 A g^{-1} over 500 cycles.

homogeneous metal growth on their surface.

SMHCs were assembled using C-CNTPs and N-PPts-0.75 as the anode and cathode, respectively, and operated in a voltage window of 1.0–4.0 V. For charge balance, the C-CNTPs were pre-sodiated after pre-cycling [Fig. 5(a)]. The full cells composed of the pre-sodiated C-CNTP anode and N-PPts-0.75 cathode had an open circuit voltage of ~2.7 V. During galvanostatic charging, the voltage of N-PPts-0.75 increased, whereas C-CNTPs showed a voltage plateau around 0 V. When the voltage gap reached 4.0 V, galvanostatic discharge proceeded until the cut-off cell voltage of 1 V. Because the energy gap between the anode and the cathode was controlled by pre-sodiation (charge injection), the full cells showed a good energy balance during the cycling process. Galvanostatic charge/discharge profiles of the SMHCs are shown in Fig. 5(b). The typical capacitive charge storage behavior, represented as a triangle, could be confirmed in the profiles. The specific cell capacitance of the SMHC was 124 F g^{-1} at a current rate of 0.2 A g^{-1}, corresponding to a specific capacity of 103 mA h g^{-1}. The reversible cell capacities gradually decreased to 94.5, 84.8, 76.3, 65.5, 56.2, and 41.7 mA h g^{-1} when the current rates were increased to 0.4, 0.7, 1, 1.5, 2, and 3 A g^{-1}, respectively [Fig. 5(c)]. Accordingly, the operating cell voltage also decreased with increasing ohmic drop, leading to gradual loss of both specific energy and power. Based on the operating cell voltage value of 2.31 V at 0.2 A g^{-1}, the specific energy was calculated to be 237.7 Wh kg^{-1} at a specific power of 462 W kg^{-1}. The maximum specific power achieved was 4800 W kg^{-1} at a current rate of 3 A g^{-1}. The specific energy vs. power relationship is depicted as a Ragone plot in Fig. 5(d). The SMHCs showed the highest specific energy and power values with the following configurations: CNP-1400//Na$_{1.5}$VPO$_{4.8}$F$_{0.7}$ [36], PCN-2800//HN-PP [37], Graphite//H-NP [30], and 3DFC//3DFAC [38], TiO$_2$@CNT@C//BAC [39]. In addition, the SMHCs showed excellent cycling performance [Fig. 5(e)]. After 500 galvanostatic charge/discharge cycles, a capacity retention of 82% was achieved, demonstrating their practical significance.

4. Conclusion

In summary, N-PPts and C-CNTPs were prepared from natural polymers by controlled pyrolysis for use as metal anodes and capacitive cathodes, respectively, to achieve high-performance SMHCs. N-PPts possessed a significantly high specific surface area of 4216 m^2 g^{-1} and nanopore volume of 1.937 cm^3 g^{-1}, showing a high specific capacity and rate capability and stable cycling performance. In addition, well-ordered C-CNTPs guided the homogeneous sodium metal plating/stripping behaviors, achieving an average CE of ~100% and standard CE deviation of ~0.51% over 1000 cycles. The SMHCs were assembled using sodiated C-CNTPs as the anode and N-PPts as the cathode and were operated in a voltage window of 1.0–4.0 V. These SMHCs achieved a high specific energy of 237.7 Wh kg^{-1} at 462 W kg^{-1} and maximum power of 4800 W kg^{-1} at 66.7 Wh kg^{-1}. In addition, a capacity retention of 82% was attained after 500 cycles.

Appendix A. Supplementary data

Supplementary data to this article can be found online at https://doi.org/10.1016/j.jpowsour.2019.02.047.

References

[1] S. Chu, A. Majumdar, Opportunities and challenges for a sustainable energy future, Nature 488 (7411) (2012) 294–303.
[2] D. Larcher, J.-M. Tarascon, Towards greener and more sustainable batteries for electrical energy storage, Nat. Chem. 7 (1) (2015) 19–29.
[3] Z.P. Cano, D. Banham, S. Ye, A. Hintennach, J. Lu, M. Fowler, Z. Chen, Batteries and fuel cells for emerging electric vehicle markets, Nat. Energy 3 (4) (2018) 279–289.
[4] B. Dunn, H. Kamath, J.-M. Tarascon, Electrical energy storage for the grid: a battery of choices, Science 334 (6058) (2011) 928–935.
[5] N. Yabuuchi, K. Kubota, M. Dahbi, S. Komaba, Research development on sodium-ion batteries, Chem. Rev. 114 (23) (2014) 11636–11682.
[6] H. Kim, H. Kim, Z. Ding, M.H. Lee, K. Lim, G. Yoon, K. Kang, Recent progress in electrode materials for sodium-ion batteries, Adv. Energy Mater. 6 (19) (2016) 1600943.

[7] Y.S. Yun, Y.-U. Park, S.-J. Chang, B.H. Kim, J. Choi, J. Wang, D. Zhang, P.V. Braun, H.-J. Jin, K. Kang, Crumpled graphene paper for high power sodium battery anode, Carbon 99 (2016) 658–664.

[8] Z.W. Seh, J. Sun, Y. Sun, Y. Cui, A Highly reversible room-temperature sodium metal anode, ACS Cent. Sci. 1 (8) (2015) 449–455.

[9] R. Cao, K. Mishra, X. Li, J. Qian, M.H. Engelhard, M.E. Bowden, K.S. Han, K.T. Mueller, W.A. Henderson, J.-G. Zhang, Enabling room temperature sodium metal batteries, Nanomater. Energy 30 (2016) 825–830.

[10] H.J. Yoon, N.R. Kim, H.-J. Jin, Y.S. Yun, Macroporous catalytic carbon nanotemplates for sodium metal anodes, Adv. Energy Mater. 8 (6) (2018) 1701261.

[11] K.J. Harry, D.T. Hallinan, D.Y. Parkinson, A.A. MacDowell, N.P. Balsara, Detection of subsurface structures underneath dendrites formed on cycled lithium metal electrodes, Nat. Mater. 13 (1) (2014) 69–73.

[12] F. Ding, W. Xu, G.L. Graff, J. Zhang, M.L. Sushko, X. Chen, Y. Shao, M.H. Engelhard, Z. Nie, J. Xiao, X. Liu, P.V. Sushko, J. Liu, J.-G. Zhang, Dendrite-free lithium deposition via self-healing electrostatic shield mechanism, J. Am. Chem. Soc. 135 (11) (2013) 4450–4456.

[13] D. Lin, Y. Liu, Z. Liang, H.-W. Lee, J. Sun, H. Wang, K. Yan, J. Xie, Y. Cui, Layered reduced graphene oxide with nanoscale interlayer gaps as a stable host for lithium metal anodes, Nat. Nanotechnol. 11 (7) (2016) 626–632.

[14] Y. Zhang, J. Qian, W. Xu, S.M. Russell, X. Chen, E. Nasybulin, P. Bhattacharya, M.H. Engelhard, D. Mei, R. Cao, F. Ding, A.V. Cresce, K. Xu, J.-G. Zhang, Dendrite-free lithium deposition with self-aligned nanorod structure, Nano Lett. 14 (12) (2014) 6889–6896.

[15] W. Li, H. Yao, K. Yan, G. Zheng, Z. Liang, Y.-M. Chiang, Y. Cui, The synergetic effect of lithium polysulfide and lithium nitrate to prevent lithium dendrite growth, Nat. Commun. 6 (2015) 7436.

[16] R. Miao, J. Yang, Z. Xu, J. Wang, Y. Nuli, L. Sun, A new ether-based electrolyte for dendrite-free lithium-metal based rechargeable batteries, Sci. Rep. 6 (2016) 21771.

[17] N.-W. Li, Y.-X. Yin, C.-P. Yang, Y.-G. Guo, An artificial solid electrolyte interphase layer for stable lithium metal anodes, Adv. Mater. 28 (9) (2016) 1853–1858.

[18] J. Song, G. Jeong, A.-J. Lee, J.H. Park, H. Kim, Y.-J. Kim, Dendrite-free polygonal sodium deposition with excellent interfacial stability in a NaAlCl$_4$–2SO$_2$ inorganic electrolyte, ACS Appl. Mater. Interfaces 7 (49) (2015) 27206–27214.

[19] K. Zhang, G.-H. Lee, M. Park, W. Li, Y.-M. Kang, Recent developments of the lithium metal anode for rechargeable non-aqueous batteries, Adv. Energy Mater. 6 (20) (2016) 1600811.

[20] R. Zhang, X.-R. Chen, X. Chen, X.-B. Cheng, X.-Q. Zhang, C. Yan, Q. Zhang, Lithiophilic sites in doped graphene guide uniform lithium nucleation for dendrite-free lithium metal anodes, Angew. Chem. Int. Ed. 56 (27) (2017) 7764–7768.

[21] A.P. Cohn, N. Muralidharan, R. Carter, K. Share, C.L. Pint, Anode-free sodium battery through in situ plating of sodium metal, Nano Lett. 17 (2) (2017) 1296–1301.

[22] P. Simon, Y. Gogotsi, Materials for electrochemical capacitors, Nat. Mater. 7 (11) (2008) 845–854.

[23] Y.S. Yun, S.Y. Cho, J. Shim, B.H. Kim, S.-J. Chang, S.J. Baek, Y.S. Huh, Y. Tak, Y.W. Park, S. Park, H.-J. Jin, Microporous carbon nanoplates from regenerated silk proteins for supercapacitors, Adv. Mater. 25 (14) (2013) 1993–1998.

[24] Y.S. Yun, G. Yoon, K. Kang, H.-J. Jin, High-performance supercapacitors based on defect-engineered carbon nanotubes, Carbon 80 (2014) 246–254.

[25] J. Chmiola, G. Yushin, Y. Gogotsi, C. Portet, P. Simon, P.L. Taberna, Anomalous increase in carbon capacitance at pore sizes less than 1 nanometer, Science 313 (5794) (2006) 1760–1763.

[26] J. Huang, B.G. Sumpter, V. Meunier, Theoretical model for nanoporous carbon supercapacitors, Angew. Chem. Int. Ed. 47 (3) (2008) 520–524.

[27] C. Merlet, B. Rotenberg, P.A. Madden, P.-L. Taberna, P. Simon, Y. Gogotsi, M. Salanne, On the molecular origin of supercapacitance in nanoporous carbon electrodes, Nat. Mater. 11 (4) (2012) 306–310.

[28] C. Merlet, C. Péan, B. Rotenberg, P.A. Madden, B. Daffos, P.-L. Taberna, P. Simon, M. Salanne, Highly confined ions store charge more efficiently in supercapacitors, Nat. Commun. 4 (2013) 2701.

[29] N.R. Kim, S.M. Lee, M.W. Kim, H.J. Yoon, W.G. Hong, H.J. Kim, H.J. Choi, H.-J. Jin, Y.S. Yun, Amphicharge-storable pyropolymers containing multitiered nanopores, Adv. Energy Mater. 7 (19) (2017) 1700629.

[30] S.Y. Cho, H.J. Yoon, N.R. Kim, Y.S. Yun, H.-J. Jin, Sodium-ion supercapacitors based on nanoporous pyroproteins containing redox-active heteroatoms, J. Power Sources 329 (2016) 536–545.

[31] Y.S. Yun, H. Bak, H.-J. Jin, Porous carbon nanotube electrodes supported by natural polymeric membranes for PEMFC, Synth. Met. 160 (7–8) (2010) 561–565.

[32] S.Y. Cho, Y.S. Yun, S. Lee, D. Jang, K.-Y. Park, J.K. Kim, B.H. Kim, K. Kang, D.L. Kaplan, H.-J. Jin, Carbonization of a stable β-sheet-rich silk protein into a pseudographitic pyroprotein, Nat. Commun. 6 (2015) 7145.

[33] X. Wang, X. Li, L. Zhang, Y. Yoon, P.K. Weber, H. Wang, J. Guo, H. Dai, N-doping of graphene through electrothermal reactions with ammonia, Science 324 (5928) (2009) 768–771.

[34] L.L. Zhang, X. Zhao, H. Ji, M.D. Stoller, L. Lai, S. Murali, S. Mcdonnell, B. Cleveger, R.M. Wallace, R.S. Ruoff, Nitrogen doping of graphene and its effect on quantum capacitance, and a new insight on the enhanced capacitance of N-doped carbon, Energy Environ. Sci. 5 (11) (2012) 9618–9625.

[35] P. Altimari, F. Pagnanelli, Electrochemical nucleation and three-dimensional growth of metal nanoparticles under mixed kinetic-diffusion control: model development and validation, Electrochim. Acta 206 (2016) 116–126.

[36] Y.S. Yun, K.-Y. Park, B. Lee, S.Y. Cho, Y.-U. Park, S.J. Hong, B.H. Kim, H. Gwon, H. Kim, S. Lee, Y.W. Park, H.-J. Jin, K. Kang, Sodium-ion storage in pyroprotein-based carbon nanoplates, Adv. Mater. 27 (43) (2015) 6914–6921.

[37] S.Y. Cho, M. Kang, J. Choi, M.E. Lee, H.J. Yoon, H.J. Kim, C. Leal, S. Lee, H.-J. Jin, Y.S. Yun, Pyrolytic carbon nanosheets for ultrafast and ultrastable sodium-ion storage, Small 14 (17) (2018) 1703043.

[38] B. Yang, J. Chen, S. Lei, R. Guo, H. Li, S. Shi, X. Yan, Spontaneous growth of 3D framework carbon from sodium citrate for high energy- and power-density and long-life sodium-ion hybrid capacitors, Adv. Energy Mater. 8 (10) (2017) 1702409.

[39] Y.-E. Zhu, L. Yang, J. Sheng, Y. Chen, H. Gu, J. Wei, Z. Zhou, Fast sodium storage in TiO$_2$@CNT@C nanorods for high-performance Na-ion capacitors, Adv. Energy Mater. 7 (22) (2017) 1701222.